

# Preparation and characterization of PANI/MWCNT/RGO ternary composites as electrode materials for supercapacitors

**Huimin Dai**

Sichuan University

**Li Rong**

Sichuan University

**Siyu Su**

Sichuan University

**Yifan Cui**

Sichuan University

**Yueming Lin**

Sichuan University

**Liang Zhang**

Sichuan University

**Xiaohong Zhu** (✉ [xhzhu@scu.edu.cn](mailto:xhzhu@scu.edu.cn))

Sichuan University <https://orcid.org/0000-0002-5772-8516>

---

## Research Article

**Keywords:** Graphene, PANI, MWCNT, Hydrothermal, Supercapacitor

**Posted Date:** June 14th, 2021

**DOI:** <https://doi.org/10.21203/rs.3.rs-611610/v1>

**License:** © ⓘ This work is licensed under a Creative Commons Attribution 4.0 International License.

[Read Full License](#)

---

**Version of Record:** A version of this preprint was published at Journal of Electronic Materials on January 11th, 2022. See the published version at <https://doi.org/10.1007/s11664-021-09421-6>.

# **Preparation and characterization of PANI/MWCNT/RGO ternary composites as electrode materials for supercapacitors**

Huimin Dai, Li Rong, Siyu Su, Yifan Cui, Yueming Lin, Liang Zhang, Xiaohong Zhu\*

*College of Materials Science and Engineering, Sichuan University, Chengdu 610064, P. R. China*

\*Corresponding author. E-mail address: xhzhu@scu.edu.cn (X. Zhu).

## **Abstract**

Electrode materials for supercapacitors are being extensively studied at present, the structural and electrochemical properties of which are still required to be further improved. Hence, a series of polyaniline/reduced graphene oxide binary composites (PANI/RGO, PG-i,  $i=2, 4, 5$ ) and polyaniline/multi-walled carbon nanotubes/reduced graphene oxide ternary composites (PANI/MWCNT/RGO, PCG-i,  $i=2, 4, 5$ ) were prepared by a facile hydrothermal method. The morphology, structure and electrochemical performance of these samples are systematically analyzed and discussed. Analysis exhibits that all the samples have abundant pore structure. By changing the ratio of components, PCG-5 shows superior comprehensive electrochemical performance, including a high specific capacitance of  $478 \text{ F g}^{-1}$  at  $1 \text{ A g}^{-1}$ , a considerable capacitance retention (63.56%, from 1 to  $20 \text{ A g}^{-1}$ , and 55.33%, from 1 to  $50 \text{ A g}^{-1}$ ) and an extraordinary cycling stability (66.28% after 3500 cycles, at  $2 \text{ A g}^{-1}$ ) in  $1 \text{ M H}_2\text{SO}_4$ . The results prove that the PANI/MWCNT/RGO ternary composite has great potential as supercapacitor electrodes.

**Key words:** Graphene; PANI; MWCNT; Hydrothermal; Supercapacitor

## 1. Introduction

In order to meet the needs of practical applications, neotype energy storage devices and equipments are constantly being studied. Supercapacitor (SC), namely electrochemical capacitor, is a kind of large-capacity capacitor between conventional batteries and capacitors. SCs are favored by various researches [1-11] because of their high power density, superior cycle stability, safety in use and fast charge-discharge characteristics. The energy storage mechanism of SCs can be classified into two categories, including electric double layer capacitor (EDLC) and pseudo-capacitor [1, 12-14]. The former stores energy through charge accumulation in the double Helmholtz layer at the interface between the working electrode and electrolyte, while the latter stores energy through Faradic process on the surface of electrode material, including ion intercalation and de-intercalation and charge transfer process among atoms on the surface [13-16].

Polyaniline (PANI), a typical pseudo-capacitance electrode material, is also one of the conductive polymers (CPs) that have been widely studied so far. It has the advantages of high conductivity, high specific capacitance, good intrinsic flexibility and simple preparation [17, 18]. However, as continuous charge and discharge might cause the structural degradation of the PANI chains (*e.g.* volumetric expansion) [19, 20], the rate performance and cycle life of pure PANI are severely limited. Therefore, to overcome these shortcomings, it is usually used in combination with other more stable materials, such as carbon materials and transition metal oxides [21-29]. For example, Dai *et al.* prepared a reduced graphene oxide/polyaniline hollow sphere composite

material (RGO/PANI-HS), which exhibited a specific capacitance of  $529 \text{ F g}^{-1}$  at  $0.5 \text{ A g}^{-1}$  [27]. Sardana *et al.* successfully synthesized PANI/MWCNT composite hydrogels on carbon cloth by in-situ oxidative polymerization, exhibiting a specific capacitance of  $277.59 \text{ F g}^{-1}$  at  $0.25 \text{ A g}^{-1}$  [28]. Han *et al.* prepared PANI/CNT/graphene on a flexible ITO/PET substrate and the sample showed a specific capacitance of  $133.45 \text{ F g}^{-1}$  at the scan rate of  $100 \text{ mV s}^{-1}$  [29].

Graphene is a particularly attractive carbon material in the field of SCs because it has a unique two-dimensional (2D) honeycomb structure, a high theoretical specific surface area up to  $2630 \text{ m}^2 \text{ g}^{-1}$ , excellent electrical conductivity and superior mechanical properties [30, 31]. Its preparation methods mainly include mechanical peeling method, redox method and chemical vapor deposition (CVD) method. Among them, the method of oxidizing graphite powder to graphene oxide (GO) and then hydrothermally reducing the graphene oxide is more commonly used because of its simple operation and low cost. However, due to the Van Der Waals force between the layers, the reduced graphene oxide (rGO) is easily stacked and agglomerated, which brings only  $100\sim 200 \text{ F g}^{-1}$  of specific capacitance that can be obtained in reality [22, 32].

Multi-walled carbon nanotubes (MWCNT) possess high specific surface area ( $1600 \text{ m}^2 \text{ g}^{-1}$ ), good stability and high electrical conductivity ( $105 \text{ S cm}^{-1}$ ) [33, 34]. According to previous reports, when MWCNT is used as a supercapacitor electrode material, its experimental intrinsic capacitance is relatively low ( $4\sim 135 \text{ F g}^{-1}$ ) [35]. This is because of the limitations of microspores and internal resistance [33, 36].

Taking the structure stability and the unique nano-scale three-dimensional winding structure into account, MWCNT can insert into graphene sheets and reducing graphene agglomeration effectively. For example, Kumar *et al.* prepared rGO/MWCNT film (GP10C) successfully using a self-assembly plus reduction method, which showed a specific capacitance of  $200 \text{ F g}^{-1}$  at  $0.25 \text{ A g}^{-1}$  [37].

After considering comprehensively, a simple one-step hydrothermal method was used to prepare PANI/RGO binary composites and PANI/MWCNT/RGO ternary composites in this work. It is expected that the three components can exert a positive synergistic effect to maximize strengths and avoid drawbacks. Graphene and MWCNT can slow down the structural collapse of PANI chains and extend the cycle life of composite. At the same time, PANI can provide composite materials with high pseudo-capacitance. In the present work, the morphology, structure and electrochemical performance of these samples are mainly discussed and analyzed.

## **2. Experimental**

### **2.1. Materials**

Graphite powder (99.95 wt%, 325 mesh; Qingdao, China), PANI (98 wt% purity, Sinopharm, China) and MWCNT (95 wt% purity; length, 0.5-2  $\mu\text{m}$ ; diameter, 10-20 nm; XFNANO, China) were used in this work. All reagents and materials were used without further purification.

### **2.2. Preparation**

Graphene oxide (GO) was prepared in advance by a modified Hummers' method.

Then 0.05 g freeze-dried GO aerogel was weighed and dissolved in 50 ml deionized water (DI water). After that, 0.5 g thiourea ( $\text{CS}(\text{NH}_2)_2$ ), 0.02 g MWCNT and  $X$  g dark green PANI powder ( $X = 0.02, 0.04, 0.05$ ) were added into GO solution with continuous stirring. Subsequently, the mixture was transferred into hydrothermal kettles to react at  $180\text{ }^\circ\text{C}$  for 12 h. After the reactor was cooled naturally, the obtained black hydrogels were filtered and washed for several times with DI water. Lastly, these PANI/MWCNT/RGO composites were freeze-dried under vacuum for 24 h, and they were named as PCG- $i$  ( $i = 2, 4, 5$ ). Furthermore, for comparison, MWCNT/RGO composite without PANI, graphene reduced only by  $\text{CS}(\text{NH}_2)_2$  and PANI/RGO composites without MWCNT were prepared according to the above steps, and they were marked as MCG, RGO and PG- $i$  ( $i = 2, 4, 5$ ), respectively.

To test these samples' electrochemical performance, a series of working electrodes were made by a simple method. These samples were dispersed in ethanol (EtOH) by ultrasonic directly, and the dispersion was coated on cleaned carbon cloth (CC) and dried at  $60\text{ }^\circ\text{C}$  for several times.

### **2.3. Characterization**

Scanning electron microscopy (SEM) (JSM-7500F, Japan) was used to probe surface morphology of these samples. X-ray diffraction (XRD) (DX-1000, China) with  $\text{Cu K}\alpha$  radiation was used to characterize the crystalline structure. Raman spectroscopy (RS) (LabRAM HR, France) with 532.17 nm laser was used to analyze the changes in the micro-structure of these samples. A mercury intrusion porosimeter (MIP) (Autopore IV 9500, USA) was used to measure the pore-size distribution. Valence analyses were

carried out using X-ray photoelectron spectrometry (XPS) (AXIS Supra (Kratos), USA) and the charge calibration was carried out with the C 1s peak with binding energy of 284.6 eV. Electrochemical tests, including cyclic voltammetry curves (CV), galvanostatic charge/discharge curves (GCD) and electrochemical impedance spectroscopy curves (EIS) ( $10^6 \sim 10^{-2}$  Hz) were carried out by an electrochemical workstation (CHI660E, China). In the three-electrode system, Hg/Hg<sub>2</sub>SO<sub>4</sub> electrode and platinum foil electrode were served as the reference electrode and counter electrode, respectively. And the electrode to be tested was used as the working electrode. All electrochemical tests were performed in 1 M H<sub>2</sub>SO<sub>4</sub> electrolyte.

### 3. Results and discussion

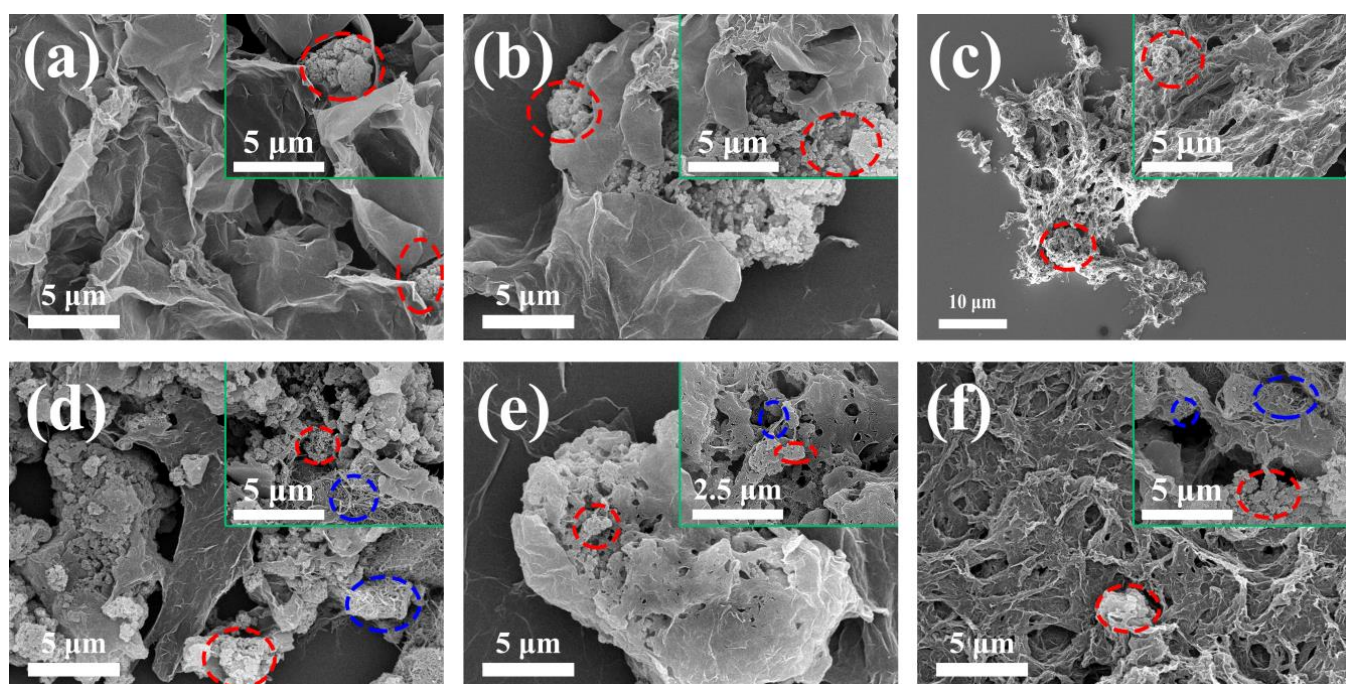


Fig. 1. SEM images of PG-i ( $i = 2, 4, 5$ ) (a-c) and PCG-i ( $i = 2, 4, 5$ ) (d-f).

From Fig. 1, PANI (circled in red), MWCNT (circled in blue) and thin wrinkled graphene sheets can be observed, indicating that PG-i and PCG-i materials have been

successfully prepared. The relatively small PANI particles (Fig. S1a) and MWCNT (Fig. S1b) are wrapped or embedded in large graphene sheets tightly. Because these composites are freeze-dried, they all exhibit abundant pore structures, especially on the micrometer scale, which are beneficial to the diffusion of ions and the infiltration of the electrolyte to the working electrode. In addition, compared to PG-*i*, the three-dimensional network structure of MWCNT introduced in PCG-*i* may buffer and reduce the volume change and structural collapse of materials during charging and discharging process, which can promote the transport of ions and electrons. However, the uneven distribution of the components can also be observed (especially in PCG-4), which may adversely affect the electrochemical performance of PCG-*i*.

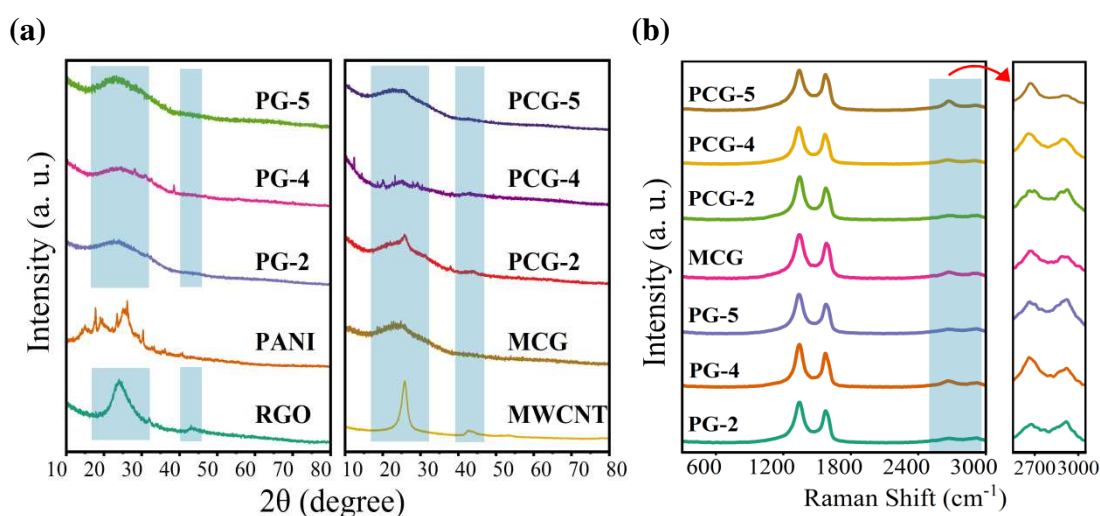


Fig. 2. XRD patterns of RGO, PANI, MWCNT, MCG, PG-*i* (*i* = 2, 4, 5) and PCG-*i* (*i* = 2, 4, 5) (a), and Raman spectra of PG-*i* (*i* = 2, 4, 5), MCG and PCG-*i* (*i* = 2, 4, 5) (b).

Fig. 2a exhibits the XRD patterns of RGO, PANI, MWCNT, MCG, PG-*i* (*i* = 2, 4, 5) and PCG-*i* (*i* = 2, 4, 5). For intrinsic PANI, its characteristic peaks are  $2\theta = 14.77^\circ$ ,  $2\theta = 19.62^\circ$ ,  $2\theta = 25.52^\circ$ , and their corresponding crystalline planes are (0 1 0), (1 0 0),

(1 1 0) respectively [38]. The peak at  $19.62^\circ$  is attributed to the alternating polyaniline chain layers, the peak at  $14.77^\circ$  is related to periodicity parallel to polyaniline chains and the peak at  $25.52^\circ$  is related to periodicity perpendicular to polyaniline chains [39]. Generally speaking, the characteristic peak positions of RGO and MWCNT in XRD patterns are about  $2\theta = 26^\circ$  and  $2\theta = 43^\circ$ , which are corresponded to (0 0 2) and (1 0 0) crystalline planes respectively. And as a result of the overlap of the peaks in the range of  $2\theta = 20 \sim 30^\circ$ , the characteristic peak of these composites at  $2\theta = 25^\circ$  is wider and more diffuse than that of pure RGO and MWCNT, indicating that these composites possess large lattice defects and a large degree of disorder.

Raman spectroscopy of MCG, PG-i ( $i = 2, 4, 5$ ) and PCG-i ( $i = 2, 4, 5$ ) is shown in Fig. 2b. These composites exhibit two conspicuous bands, namely D band ( $\sim 1350 \text{ cm}^{-1}$ ) and G band ( $\sim 1592 \text{ cm}^{-1}$ ). The D band is the disordered vibration peak of graphene, which represents the defects in the graphene. The G band is caused by the in-plane vibration of  $\text{sp}^2$  carbon atoms, which can represent the crystal phase structure of graphene. In addition, the 2D band ( $\sim 2700 \text{ cm}^{-1}$ ) is attributed to the double resonance transition of two phonons with opposite momentum in the graphene carbon atom [5, 40]. Raman  $I_D/I_G$  value (where  $I_D$  and  $I_G$  are the intensity of D band and G band) is usually used to measure defect richness in graphene, which can be used as a rough reference for comparing the conductivity of materials. This is because lattice defects are conducive to the transmission of ions, while they result in poor electronic conductivity. Table 1 lists the detailed data of PG-i ( $i = 2, 4, 5$ ), MCG and PCG-i ( $i = 2, 4, 5$ ). Although PCG-5 has the least defects and the transmission of ions may be

limited, it can be considered that its electronic conductance is the highest among several groups.

Table 1. The position of D band, the position of G band and the value of  $I_D/I_G$  of PG-i (i = 2, 4, 5),

MCG and PCG-i (i = 2, 4, 5).

Sample	PG-2	PG-4	PG-5	MCG	PCG-2	PCG-4	PCG-5
D band ( $\text{cm}^{-1}$ )	1342.14	1341.45	1340.17	1343.48	1343.89	1337.72	1344.74
G band ( $\text{cm}^{-1}$ )	1572.45	1573.91	1574.61	1578.75	1574.12	1568.24	1574.21
$I_D/I_G$	1.19	1.22	1.26	1.17	1.29	1.16	0.98

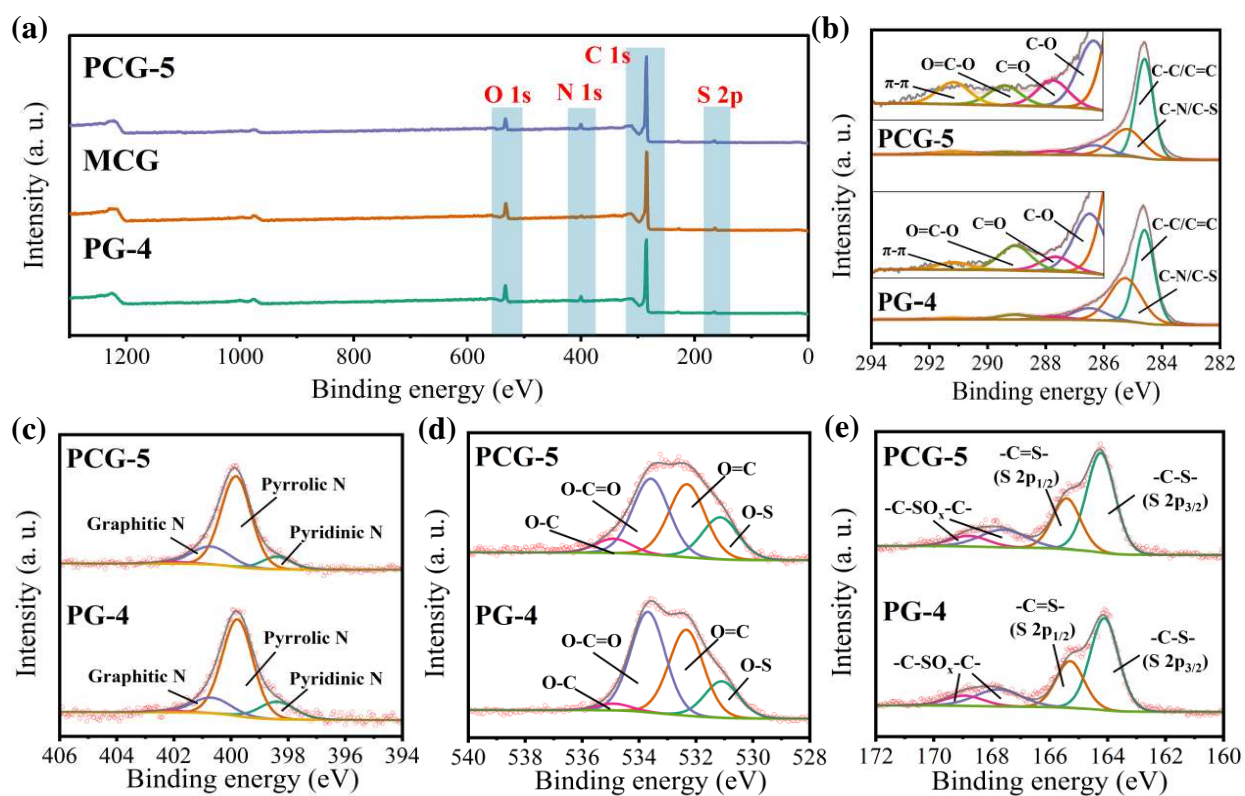


Fig. 3. XPS survey spectra of PG-4, MCG and PCG-5 (a), the high-resolution C 1s spectra (b), the

high-resolution N 1s spectra (c), the high-resolution O 1s spectra (d), the high-resolution S 2p spectra (e) of PG-4 and PCG-5.

Valence analysis were carried out by XPS, and the fitted results are displayed in Fig. 3 and Fig. S2. Thiourea is used as both nitrogen source and carbon source, and PANI is another nitrogen source during hydrothermal reactions, so the area of N 1s region of MCG in the survey spectra is obviously smaller than that of PG-4 and PCG-5. The high-resolution C 1s spectrum of PG-4 and PCG-5 can be well fitted to six parts, including C-C (284.60 eV), C-N/C-S (285.21 eV), C-O (286.32 eV), C=O (287.74 eV), -COOH (289.42 eV) and  $\pi$ - $\pi$  conjugation (291.20 eV). The high-resolution N 1s spectrum can be fitted into three parts, namely pyridinic N (398.39 eV), pyrrolic N (399.82 eV) and graphitic N (400.72 eV). The existence of graphitic N proves that N element has been doped into the hexagonal structure of graphene, which can enhance conductivity and hydrophilicity of carbon composites. Pyridinic N and pyrrolic N can provide  $\pi$ -electrons to the conjugated system in graphene layers. Therefore, they will increase the specific capacitance through extra redox reactions. By comparing the area of each region, it can be seen that the relative content of pyrrolic N is the most. The O 1s high-resolution spectrum can be fitted into four parts, namely O-S (531.14 eV), O-C (532.31 eV), O-C=O (533.58 eV) and O-C (534.89 eV). The S 2p high-resolution spectrum can be divided into three parts, namely -C-S- (164.23 eV), -C=S- (165.41 eV) and -C-SO<sub>x</sub>-C-, respectively. The first two S-contained groups (thiophene-like S) can enhance conductivity, and the third S-contained group (oxidized S) can participate

in the Faradic reaction in liquid electrolyte to provide pseudo-capacitance [41].

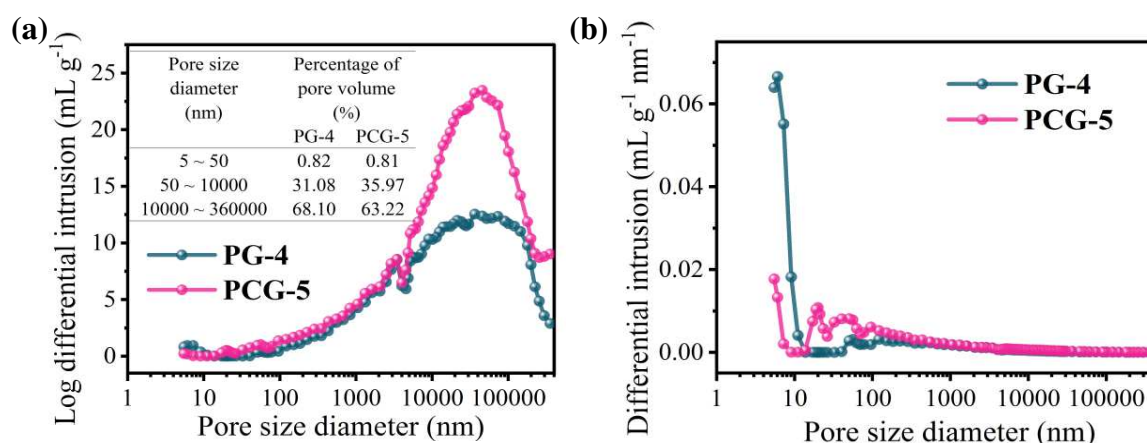


Fig. 4. Pore-size distribution (a), and pore length distribution (b) of PG-4 and PCG-5.

Table 2. MIP data analysis of PG-4 and PCG-5.

Sample	Total intrusion volume (mL g <sup>-1</sup> )	Total pore area (m <sup>2</sup> g <sup>-1</sup> )	Median pore diameter (volume) (nm)	Median pore diameter (area) (nm)	Average pore diameter (nm)	Bulk density (g mL <sup>-1</sup> )	Porosity (%)
PG-4	25.65	154.53	20299.10	7.22	663.99	0.3197	89.13
PCG-5	39.14	110.87	25901.46	65.97	1412.22	0.5300	95.40

It can be seen from the SEM images that composite materials have rich pore structures, especially mesopore (2-50 nm) and macropore (>50 nm) structures. Therefore, the mercury intrusion porosimeter (MIP) method was used to analyze the distribution characteristics of mesopores and macropores. Fig. 4 is the pore size distribution diagram of PG-4 and PCG-5. The interpolated table is the pore volume percentage in different pore ranges. It can be seen that both PG-4 and PCG-5 are rich in mesopores and macropores, which is conducive to the infiltration of the sample in

the electrolyte. The samples have such rich pore structures because the vacuum freeze-drying process can keep the microstructure of the hydrogel prepared by the hydrothermal method from being damaged. Fig. 4b is a distribution diagram of the pore length ratio corresponding to the pore size, which can be used as a reference. It can be seen that in the range of <300 nm, the pore length of PG-4 and PCG-5 is longer, especially when the pore diameter is less than 10 nm. In general, the smaller the pore, the deeper the pore. It can be inferred that there are three-dimensional microporous network structures inside these samples, which may be attributed to the incorporation of PANI chains and MWCNT. This plays a crucial role in improving the capacitance. MIP data analysis of these samples are listed in Table 2 and Table S1. It can be seen that the porosity of PG-*i* (*i* = 2, 4, 5) and PCG-*i* (*i* = 2, 4, 5) are both above 89.13%, and both have a large total pore area (70~155 m<sup>2</sup> g<sup>-1</sup>). This means that there are a lot of electrochemically active sites inside these materials. Besides, these materials are directly loaded on clean carbon cloth, which reduces the damage of grinding to the microstructures. Therefore, these samples may show superior electrochemical performance.

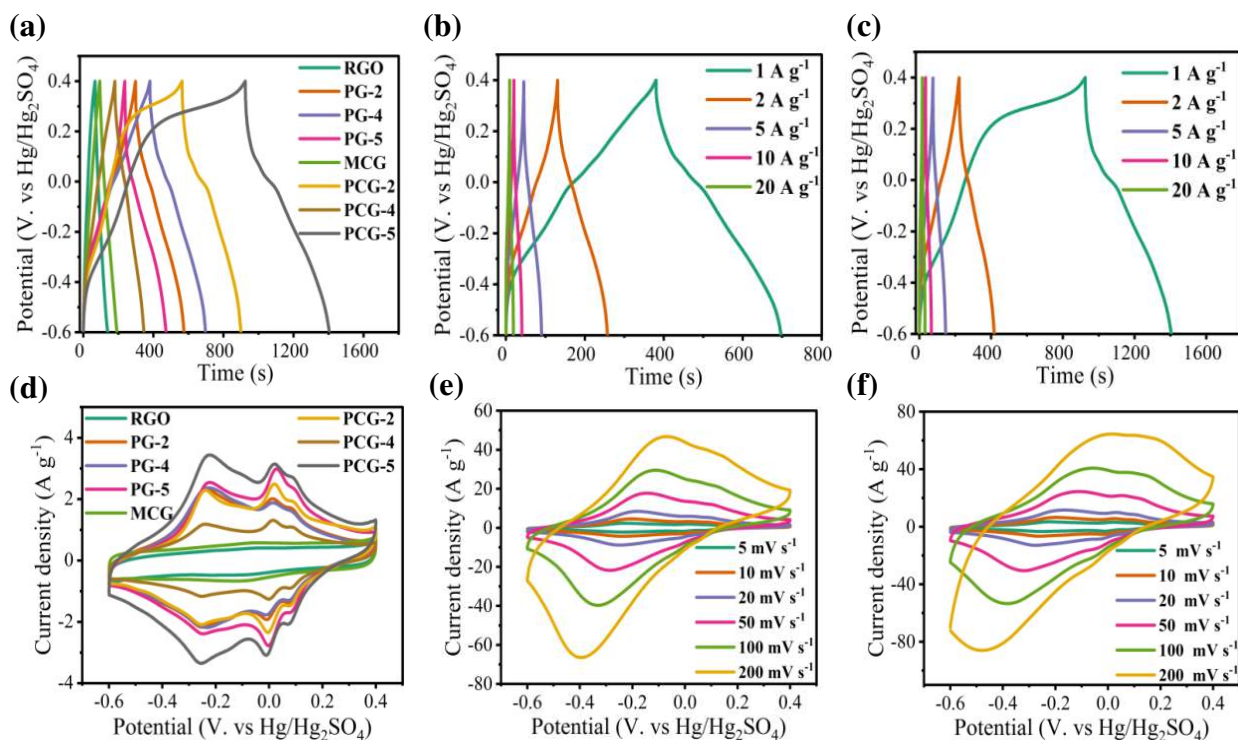


Fig. 5. GCD curves of RGO, PG-*i* (*i* = 2, 4, 5), MCG and PCG-*i* (*i* = 2, 4, 5) at 1 A g<sup>-1</sup> (a), GCD curves of PG-4 and PCG-5 at different current densities (b~c), CV curves of RGO, PG-*i* (*i* = 2, 4, 5), MCG and PCG-*i* (*i* = 2, 4, 5) at 5 mV s<sup>-1</sup> (d), CV curves of PG-4 and PCG-5 at different scan rates (e~f).

For electrochemical tests, the selected voltage window is -0.6~0.4 V. From Fig. 5, it can be seen that the capacitance of PCG-5 is the highest. According to Fig. 6d, the CV curves of RGO and MCG are similar to rectangles, while those of the other composites exhibit obvious oxidation peaks and reduction peaks, which is attributed to the doping and de-doping of counterions that occur in the PANI chains [20]. This shows that RGO and MCG mainly exhibit electric double-layer capacitance while other composites exhibit obvious pseudo-capacitance due to the incorporation of PANI. As the scan rate increases, the oxidation peak (or reduction peak) shifts slightly

to the left (or right). This is because at high scan rates, the transmission speed of electrolyte ions and the rapid transmission speed of electrons do not match the transmission speed of electrons inside or near the active material, and a large number of electrons are gathered together. Therefore, the charge potential increases and the discharge potential decreases, and the potential difference between the two redox peaks also becomes obvious. The peaks at 0.02 V and 0.07 V gradually overlap due to their close positions. PG-4 and PCG-5 are mainly compared and analyzed, because they have the highest capacitance values in their respective groups. It can be seen that the CV curves of PG-4 and PCG-5 are gradually deformed as the scan rate increases. Compared with the CV curves of PG-4, those of PCG-5 deforms more obviously, which might be due to the entanglement of MWCNT.

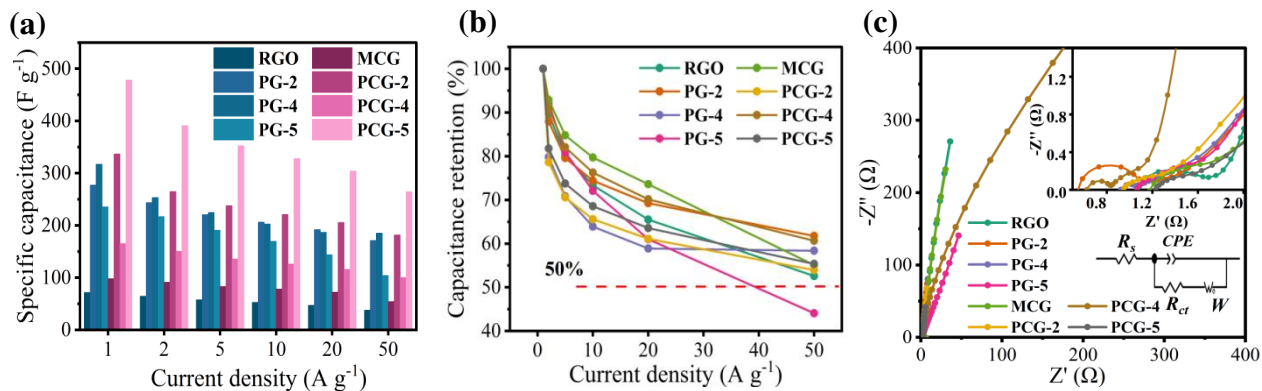


Fig. 6. The calculated  $C_m$  at different current densities (a), the capacitance retention (b), and the EIS curves (c) of RGO, MCG, PG- $i$  ( $i = 2, 4, 5$ ) and PCG- $i$  ( $i = 2, 4, 5$ ).

According to Eq. (1), the specific capacitance ( $C_m$ , F g<sup>-1</sup>) of composites can be calculated from GCD curves.

$$C_m = \frac{I \times \Delta t}{\Delta V \times m} \quad (1)$$

where  $I$ ,  $\Delta t$ ,  $\Delta V$  and  $m$  are discharge current (A), discharge time (s), potential window (V), and the mass loading of active materials (g), respectively.

The calculated specific capacitance values of RGO, MCG, PG- $i$  ( $i = 2, 4, 5$ ) and PCG- $i$  ( $i = 2, 4, 5$ ) at  $1 \text{ A g}^{-1}$  are 71.6, 97.9, 277, 317, 235.3, 336.5, 165.1 and  $478 \text{ F g}^{-1}$ , respectively, as displayed in Fig. 6a. The capacitance value of PCG-4 is abnormal compared with our expectations. It may be because of the serious uneven distribution and agglomeration of the three components. And in Fig. 6b, the capacitance retention of RGO, MCG, PG- $i$  ( $i = 2, 4, 5$ ) and PCG- $i$  ( $i = 2, 4, 5$ ) from 1 to  $20 \text{ A g}^{-1}$  are 65.50%, 73.59%, 69.24%, 58.86%, 61.03%, 61.10%, 70.14% and 63.56%, respectively. Even if the current density is increased to  $50 \text{ A g}^{-1}$ , all the samples except PG-5 can maintain above 50%. RGO does not have as good rate performance as expected, which may be related to the destruction of the structural regularity of graphene by the incorporation of N and S atoms. In some samples, the effect of this damage is partially compensated by PANI chains and MWCNT. It is found that the addition of MWCNT can obviously increase the specific capacitance and rate performance on the whole. In summary, PCG-5 has a good capacitance retention and the highest specific capacitance.

The EIS curves are illustrated in Fig. 6c. It is obvious that charge transfer process and diffusion-controlled process control the total electrode process jointly. Through the intercept on horizontal axis, the semicircle radius in the high frequency region and the slope of the straight line in the low frequency region, the equivalent series resistance ( $R_s$ ), the charge transfer resistance ( $R_{ct}$ ), and the Warburg impedance ( $W$ ) can be

gotten respectively. And the straight line is more parallel to the vertical axis; the more similar it is to an ideal supercapacitor. According to the fitting results (Table S2), the  $R_s$  values (0.56~1.24  $\Omega$ ) and  $R_{ct}$  values (0.12~0.82  $\Omega$ ) of RGO, MCG, PG- $i$  ( $i = 2, 4, 5$ ) and PCG- $i$  ( $i = 2, 4, 5$ ) are relatively low.

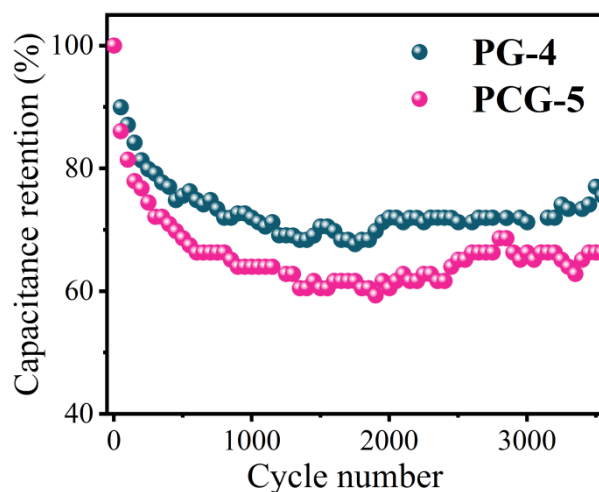


Fig. 7. Capacitance retention of PG-4 and PCG-5 after 3500 cycles of continuous charging and discharging at 2 A g<sup>-1</sup>.

According to Eq. (2) and Eq. (3), the energy density ( $E$ , Wh kg<sup>-1</sup>) and the corresponding power density ( $P$ , W kg<sup>-1</sup>) of PCG-5 can be obtained.

$$E = \frac{C_m \times \Delta V^2}{2 \times 3.6} \quad (2)$$

$$P = \frac{3600 \times E}{\Delta t} \quad (3)$$

where  $C_m$ ,  $\Delta V$ ,  $\Delta t$  are the specific capacitance of the device (F g<sup>-1</sup>), potential window (V) and discharge time (s), respectively. Accordingly, the energy density of PCG-5 is calculated as 66.39, 54.28, 48.96, 45.51, and 42.19 Wh kg<sup>-1</sup> at the corresponding power density of 0.5, 1, 2.5, 5, and 10 kW kg<sup>-1</sup>, respectively. As illustrated in Fig. 7,

The capacitance retention (at 2 A g<sup>-1</sup>) of PG-4 is 76.97% and that of PCG-5 is 66.28% after 3500 cycles of continuous charging and discharging.

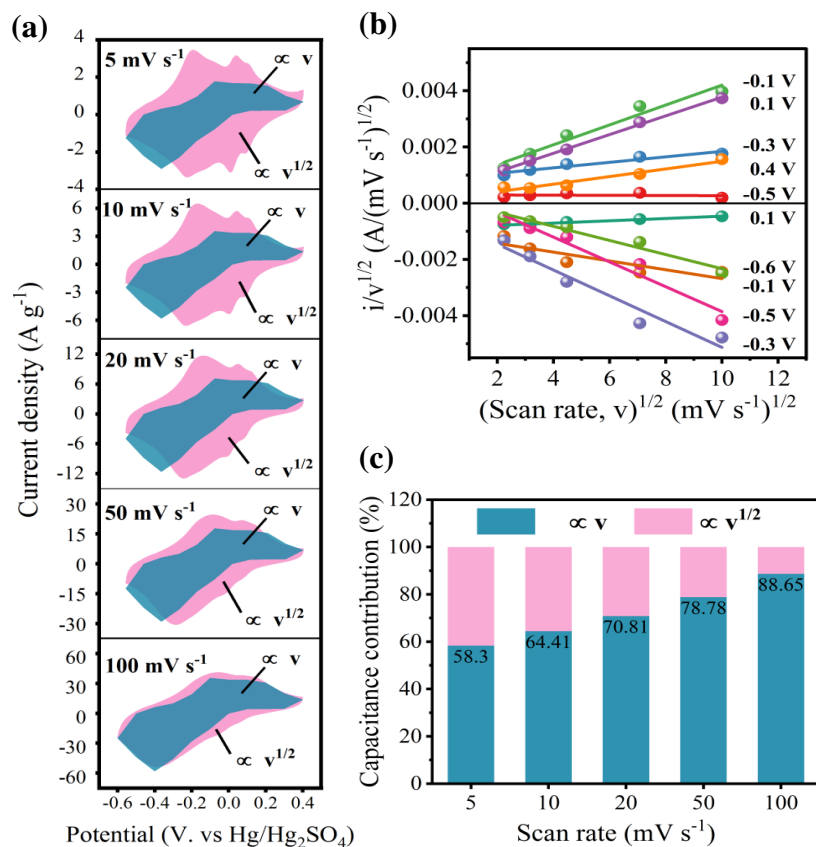


Fig. 8. Deconvoluted surface-limiting capacitance ( $\propto v$ , blue region) and diffusion-controlled capacitance ( $\propto v^{1/2}$ , purple region) of PCG-5 at different scan rates (a),  $i/v^{1/2}$  vs  $v^{1/2}$  plots of PCG-5 at different potentials (b), the contribution percentage of the capacitive and diffusion-controlled process at different scan rates of PCG-5 (c).

The capacitance contribution can be calculated roughly according to the CV curves [15, 42-45].

$$i(V) = k_1 v + k_2 v^{1/2} \quad (4)$$

Which can also be expressed as,

$$i(V)/v^{1/2} = k_1 v^{1/2} + k_2 \quad (5)$$

where  $i(V)$ ,  $k_1$  and  $k_2$  are the current at a specific potential  $V$  (V) and constants which are corresponded to the scan rate  $v$  ( $\text{mV s}^{-1}$ ) respectively. And  $k_1v$  and  $k_2v^{1/2}$  represent the current parts contributed by the surface-limiting capacitive process and the diffusion-controlled process, respectively. The values of  $k_1$  and  $k_2$  under different potentials can be obtained by the linear fitting results according to Eq. (5), where  $k_1$  is the slope of the fitted straight line and  $k_2$  is the line's intercept on the vertical axis. Theoretically, the more points are selected, the more accurate the curve will be. In this work, only a dozen points were selected as fitting points. And due to the influence of electrochemical polarization and the inherent limitations of Eq. (5), the fitting results only serve as a reference. Moreover, due to the limitation of Eq. (4), the fitting of  $k_1$  values is inaccurate (Fig. 8b), so that the fitting area contributed by the capacitance (Fig. 8a) has overflow parts. Fig. 8c is a comparison diagram of the capacitance contribution ratio and the diffusion-controlled process ratio calculated according to the area ratio of each part in Fig. 8a. As scan rate increases from 5 to 100  $\text{mV s}^{-1}$ , the capacitive process contributes 58.3%, 64.41%, 70.81%, 78.78% and 88.65% of the total capacitance while the ratio of diffusion-controlled process is gradually decreased. This might be the mismatch between the transfer rate of electrons in the external circuit and the diffusion rate of ions in the electrolyte. Totally, surface-limiting capacitance contributes the most, that is, the capacitive process of PCG-5 plays a dominant role.

All in all, the specific capacitance of PANI/MWCNT/RGO composites is higher than that of the PANI/RGO composites, and that of pure RGO is the lowest. But the

uneven distribution of components will also lead to a sharp deterioration of the specific capacitance. The uneven distribution of components in ternary materials is more obvious, so the cyclic stability of PCG-5 is slightly lower than that of PG-4, and the rate performance of each composite is not much different. Even so, PCG-5 still shows its huge research potential and application potential.

#### **4. Conclusions**

In this work, RGO, PANI/RGO (PG-*i*, *i* = 2, 4, 5) binary composites, MCG and PANI/MWCNT/RGO (PCG-*i*, *i* = 2, 4, 5) ternary composites were prepared by a simple hydrothermal method. Analysis shows that the prepared samples have abundant pore structure and specific surface area. Among them, the as-prepared PCG-5 possesses excellent comprehensive electrochemical performance. It shows a considerable specific capacitance ( $478 \text{ F g}^{-1}$  at  $1 \text{ A g}^{-1}$ ), an excellent rate capability (63.56%, from 1 to  $20 \text{ A g}^{-1}$ , and 55.33%, from 1 to  $50 \text{ A g}^{-1}$ ) and an extraordinary cycling stability (66.28% after 3500 cycles, at  $2 \text{ A g}^{-1}$ ) at positive potential window of -0.6~0.4 V. These results benefit from the structural and electrochemical synergistic effects of PANI, graphene and MWCNT. In short, PANI/MWCNT/RGO ternary composites still have great research potential, and PCG-5 can be considered as a promising electrode material for supercapacitors.

#### **Supplementary Information**

SEM images of PANI and MWCNT (Fig. S1); the high-resolution C 1s spectra, the high-resolution N 1s spectra, the high-resolution O 1s spectra and the high-resolution S 2p spectra

of MCG (Fig. S2), MIP data analysis of PG-i (i = 2, 4, 5), MCG and PCG-i (i = 2, 4, 5) (Table S1);  
the fitted  $R_s$  and  $R_{ct}$  of PG-i (i = 2, 4, 5), MCG and PCG-i (i = 2, 4, 5) (Table S2).

## References

- [1] A. Muzaffar; M.B. Ahamed; K. Deshmukh; J. Thirumalai, *Renew. Sust. Energ. Rev.* **101**, 123 (2019). <http://doi.org/10.1016/j.rser.2018.10.026>.
- [2] Poonam; K. Sharma; A. Arora; S.K. Tripathi, *J. Energy Storage* **21**, 801 (2019). <http://doi.org/10.1016/j.est.2019.01.010>.
- [3] Z.F. Yang; J.R. Tian; Z.F. Yin; C.J. Cui; W.Z. Qian; F. Wei, *Carbon* **141**, 467 (2019). <http://doi.org/10.1016/j.carbon.2018.10.010>.
- [4] C.X. Shao; T. Xu; J. Gao; Y. Liang; Y. Zhao; L.T. Qu, *Nanoscale* **9**, 12324 (2017). <http://doi.org/10.1039/c7nr04889k>.
- [5] H.L. Wang; Q.L. Hao; X.J. Yang; L.D. Lu; X. Wang, *Nanoscale* **2**, 2164 (2010). <http://doi.org/10.1039/c0nr00224k>.
- [6] T. Wang; X.B. Zang; X.M.Z. Wang; X.X. Gu; Q.G. Shao; N. Cao, *Energy Storage Mater.* **30**, 367 (2020). <http://doi.org/10.1016/j.ensm.2020.04.044>.
- [7] G.M. Zhou; L. Xu; G.W. Hu; L.Q. Ma; Y. Cui, *Chem. Rev.* **119**, 11042 (2019). <http://doi.org/10.1021/acs.chemrev.9b00326>.
- [8] Y. Wu; Z. Meng; J. Yang; Y. Xue, *Nanotechnology* **32**, (2021). <http://doi.org/10.1088/1361-6528/abf5fe>.
- [9] P.C. Du; Y.M. Dong; H.X. Kang; X. Yang; Q. Wang; J.Y. Niu; S.H. Wang; P. Liu, *ACS Sustain. Chem. Eng.* **6**, 14723 (2018). <http://doi.org/10.1021/acssuschemeng.8b03278>.
- [10] L.B. Wang; H.L. Yang; X.X. Liu; R. Zeng; M. Li; Y.H. Huang; X.L. Hu, *Angew. Chem. Int. Ed.* **56**, 1105 (2017). <http://doi.org/10.1002/anie.201609527>.
- [11] M.N. Xu; H. Guo; R. Xue; M.Y. Wang; N. Wu; X.Q. Wang; J.Y. Zhang; T.T. Zhang; W. Yang, *J. Alloys Compd.* **863**, (2021). <http://doi.org/10.1016/j.jallcom.2020.157699>.
- [12] Y.Q. Jiang; J.P. Liu, *Energy Environ. Mater.* **2**, 30 (2019). <http://doi.org/10.1002/eem2.12028>.
- [13] A.M. Bryan; L.M. Santino; Y. Lu; S. Acharya; J.M. D'Arcy, *Chem. Mater.* **28**, 5989 (2016). <http://doi.org/10.1021/acs.chemmater.6b01762>.
- [14] L.L. Zhang; X.S. Zhao, *Chem. Soc. Rev.* **38**, 2520 (2009). <http://doi.org/10.1039/b813846j>.
- [15] Y. Gogotsi; R.M. Penner, *ACS Nano* **12**, 2081 (2018). <http://doi.org/10.1021/acs.nano.8b01914>.
- [16] V. Augustyn; P. Simon; B. Dunn, *Energy Environ. Sci.* **7**, (2014). <http://doi.org/10.1039/c3ee44164d>.
- [17] M.E. Abdelhamid; A.P. O'Mullane; G.A. Snook, *RSC Adv.* **5**, 11611 (2015). <http://doi.org/10.1039/c4ra15947k>.
- [18] A. Eftekhari; L. Li; Y. Yang, *J. Power Sources* **347**, 86 (2017). <http://doi.org/10.1016/j.jpowsour.2017.02.054>.
- [19] Y.Y. Huang; J.L. Lu; S.M. Kang; D. Weng; L. Han; Y.F. Wang, *Int. J. Electrochem. Sci.*, 9298 (2019). <http://doi.org/10.20964/2019.09.86>.
- [20] T.Y. Liu; Y. Li, *InfoMat.* **2**, 807 (2020). <http://doi.org/10.1002/inf2.12105>.
- [21] J. Banerjee; K. Dutta; M.A. Kader; S.K. Nayak, *Polym. Adv. Technol.* **30**, 1902 (2019). <http://doi.org/10.1002/pat.4624>.

- [22] D. Liu; H.X. Wang; P.C. Du; W.L. Wei; Q. Wang; P. Liu, *Electrochim. Acta* **259**, 161 (2018). <http://doi.org/10.1016/j.electacta.2017.10.165>.
- [23] P.B. Liu; J. Yan; X.G. Gao; Y. Huang; Y.Q. Zhang, *Electrochim. Acta* **272**, 77 (2018). <http://doi.org/10.1016/j.electacta.2018.03.198>.
- [24] R. Pal; S.L. Goyal; I. Rawal; A.K. Gupta; Ruchi, *J. Phys. Chem. Solids* **154**, (2021). <http://doi.org/10.1016/j.jpics.2021.110057>.
- [25] D.D. Potphode; L. Sinha; P.M. Shirage, *Appl. Surf. Sci.* **469**, 162 (2019). <http://doi.org/10.1016/j.apsusc.2018.10.277>.
- [26] C.C. Wang; Y. Yang; R.J. Li; D.T. Wu; Y. Qin; Y. Kong, *Chem. Commun. (Camb.)* **56**, 4003 (2020). <http://doi.org/10.1039/d0cc01028f>.
- [27] W.Q. Dai; L. Ma; M.Y. Gan; S.Y. Wang; X.W. Sun; H.H. Wang; H.N. Wang; T. Zhou, *Mater. Res. Bull.* **76**, 344 (2016). <http://doi.org/10.1016/j.materresbull.2015.12.045>.
- [28] S. Sardana; A. Gupta; A.S. Maan; S. Dahiya; K. Singh; A. Ohlan, *Indian J. Phys.*, (2021). <http://doi.org/10.1007/s12648-020-01996-w>.
- [29] J. Han; J. Sohn; S. Cho; Y. Jo; J. Kim; H. Woo; H. Kim; A.I. Inamdar; H. Kim; H. Im, *J. Korean Phys. Soc.* **67**, 512 (2015). <http://doi.org/10.3938/jkps.67.512>.
- [30] F. Farjadian; S. Abbaspour; M.A.A. Sadatlu; S. Mirkiani; A. Ghasemi; M. Hoseini-Ghahfarokhi; N. Mozaffari; M. Karimi; M.R. Hamblin, *ChemistrySelect* **5**, 10200 (2020). <http://doi.org/10.1002/slct.202002501>.
- [31] V. Chabot; D. Higgins; A.P. Yu; X.C. Xiao; Z.W. Chen; J.J. Zhang, *Energy Environ. Sci.* **7**, (2014). <http://doi.org/10.1039/c3ee43385d>.
- [32] J. Du; L. Liu; Y.F. Yu; L.L. Zhang; Y. Zhang; A.B. Chen, *Mater. Chem. Phys.* **223**, 145 (2019). <http://doi.org/10.1016/j.matchemphys.2018.10.062>.
- [33] C.Y. Xiong; T.H. Li; T.K. Zhao; A.L. Dang; H. Li; X.L. Ji; W.B. Jin; S.S. Jiao; Y.D. Shang; Y.G. Zhang, *Compos. B. Eng.* **116**, 7 (2017). <http://doi.org/10.1016/j.compositesb.2017.02.028>.
- [34] J.B. Yang; X.X. Ji; L.B. Liu; Y. Xiang; Y.L. Zhu, *J. Alloys Compd.* **820**, (2020). <http://doi.org/10.1016/j.jallcom.2019.153081>.
- [35] S.H. Aboutalebi; A.T. Chidembo; M. Salari; K. Konstantinov; D. Wexler; H.K. Liu; S.X. Dou, *Energy Environ. Sci.* **4**, (2011). <http://doi.org/10.1039/c1ee01039e>.
- [36] A.G. Pandolfo; A.F. Hollenkamp, *J. Power Sources* **157**, 11 (2006). <http://doi.org/10.1016/j.jpowsour.2006.02.065>.
- [37] A. Kumar; N. Kumar; Y. Sharma; J. Leu; T.Y. Tseng, *Nanoscale Res. Lett.* **14**, 266 (2019). <http://doi.org/10.1186/s11671-019-3100-1>.
- [38] J.P. Pouget; M.E. Jozefowicz; A.J. Epstein; X. Tang; A.G. MacDiarmid, *Macromolecules* **24**, 779 (1991). <http://doi.org/10.1021/ma00003a022>.
- [39] Z.J. Sun; J.M. Zhang; F. Ye; W.J. Wang; G.C. Wang; Z.P. Zhang; S.L. Li; Y. Zhou; J. Cai, *J. Power Sources* **443**, (2019). <http://doi.org/10.1016/j.jpowsour.2019.227246>.
- [40] X. Li; Y. Tang; J.H. Song; W. Yang; M.S. Wang; C.Z. Zhu; W.G. Zhao; J.M. Zheng; Y.H. Lin, *Carbon* **129**, 236 (2018). <http://doi.org/10.1016/j.carbon.2017.11.099>.
- [41] L. Miao; D.Z. Zhu; M.X. Liu; H. Duan; Z.W. Wang; Y.K. Lv; W. Xiong; Q.J. Zhu; L.C. Li; X.L. Chai; L.H. Gan, *Electrochim. Acta* **274**, 378 (2018). <http://doi.org/10.1016/j.electacta.2018.04.100>.
- [42] P. Simon; Y. Gogotsi; B. Dunn, *Science* **343**, 1210 (2014). <http://doi.org/10.1126/science.1249625>.
- [43] D. Chao; C. Zhu; P. Yang; X. Xia; J. Liu; J. Wang; X. Fan; S.V. Savilov; J. Lin; H.J. Fan; Z.X.

Shen, Nat. Commun. **7**, 12122 (2016). <http://doi.org/10.1038/ncomms12122>.

[44] S.Y. Su; L.Q. Lai; R. Li; Y.M. Lin; H.M. Dai; X.H. Zhu, ACS Appl. Energy Mater. **3**, 9379 (2020). <http://doi.org/10.1021/acsaem.0c01745>.

[45] D.P. Dubal; N.R. Chodankar; D.H. Kim; P. Gomez-Romero, Chem. Soc. Rev. **47**, 2065 (2018). <http://doi.org/10.1039/c7cs00505a>.

## **Acknowledgments**

This work was financially supported by the Key Research and Development Project of Sichuan Province, China (Grant No. 2017GZ0396), Guizhou Science and Technology Program (Grant No. [2020]2Y063-2020QT) and the Fundamental Research Funds for Central Universities. The authors acknowledge the help of Hui Wang from the Analytical and Testing Center of Sichuan University for SEM analysis.

## **Author information**

### **Affiliations**

**College of Materials Science and Engineering, Sichuan University, Chengdu 610064, P. R. China**

Huimin Dai, Li Rong, Siyu Su, Yifan Cui, Yueming Lin, Liang Zhang, Xiaohong Zhu

### **Contributions**

**Huimin Dai:** Methodology, Data curation, Writing-original draft. **Li Rong:** Investigation, Methodology, Data curation, Validation. **Siyu Su:** Data curation, Supervision. **Yifan Cui:** Investigation, Supervision. **Yueming Lin:** Investigation. **Liang Zhang:** Investigation. **Xiaohong Zhu:** Methodology, Supervision, Writing-review & editing, Resources, Funding acquisition.

### **Corresponding author**

Correspondence to Xiaohong Zhu.

**Declaration of Competing Interest**

The authors declare that they have no known competing financial interests or personal relationships that could have appeared to influence the work reported in this paper.

# Preparation and characterization of PANI/MWCNT/RGO ternary composites as electrode materials for supercapacitors

Huimin Dai, Li Rong, Siyu Su, Yifan Cui, Yueming Lin, Liang Zhang, Xiaohong Zhu\*

College of Materials Science and Engineering, Sichuan University, Chengdu 610064, P. R. China

\*Corresponding author. E-mail address: xhzhu@scu.edu.cn (X. Zhu).

## Supplementary Information

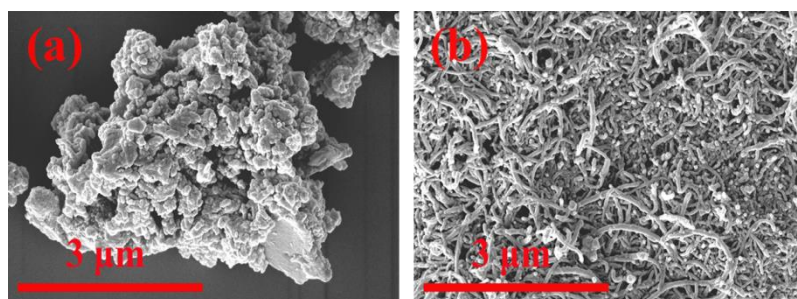


Fig. S1. SEM images of PANI (a) and MWCNT (b).

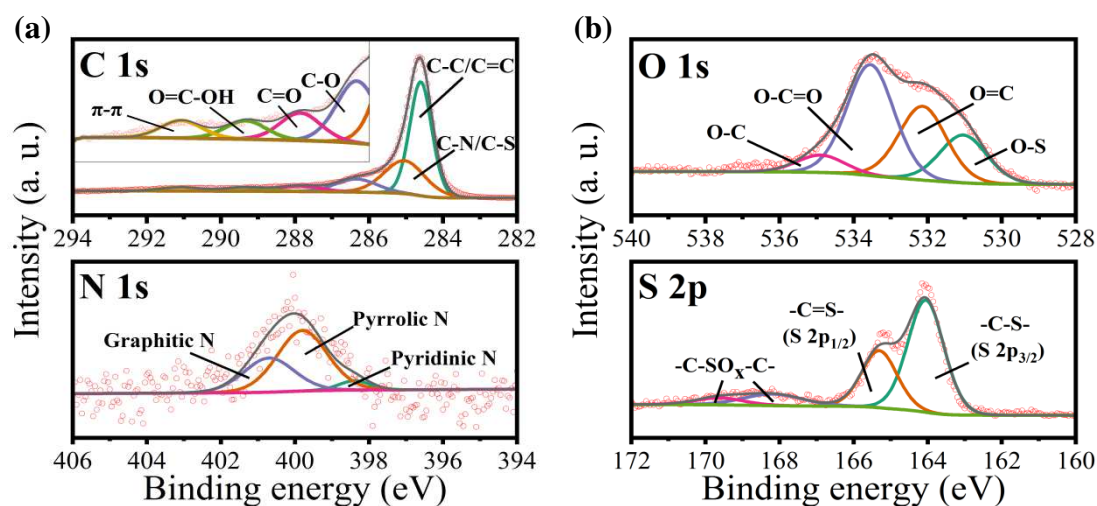


Fig. S2. The high-resolution C 1s spectra and high-resolution N 1s spectra of MCG (a), the high-resolution O 1s spectra and high-resolution S 2p spectra of MCG (b).

Table S1. MIP data analysis of PG-i (i = 2, 4, 5), MCG and PCG-i (i = 2, 4, 5).

Sample	Total intrusion volume	Total pore area (m <sup>2</sup> g <sup>-1</sup> )	Median pore diameter (volume)	Median pore diameter	Average pore diameter	Bulk density (g mL <sup>-1</sup> )	Porosity (%)
--------	------------------------	---	-------------------------------	----------------------	-----------------------	------------------------------------	--------------

	(mL g <sup>-1</sup> )		(nm)	(area) (nm)		(nm)	
PG-2	21.35	109.08	10,030.51	41.89	782.82	0.0443	94.51
PG-4	25.65	154.53	20299.10	7.22	663.99	0.3197	89.13
PG-5	25.22	155.44	19,247.81	23.15	649.05	0.0388	97.86
MCG	31.59	90.35	22,644.61	109.31	1,398.65	0.0308	97.19
PCG-2	33.67	70.15	23,596.17	187.51	1,919.69	0.0287	96.52
PCG-4	31.18	88.96	20,875.25	74.42	1,401.88	0.0305	94.96
PCG-5	39.14	110.87	25901.46	65.97	1412.22	0.5300	95.40

Table S2. The fitted  $R_s$  and  $R_{ct}$  of PG-i (i = 2, 4, 5), MCG and PCG-i (i = 2, 4, 5).

Sample	RGO	PG-2	PG-4	PG-5	MCG	PCG-2	PCG-4	PCG-5
$R_s$ ( $\Omega$ )	1.09	0.56	0.93	1.08	1.23	0.95	0.60	1.24
$R_{ct}$ ( $\Omega$ )	0.48	0.59	0.18	0.82	0.14	0.12	0.12	0.20

# Figures

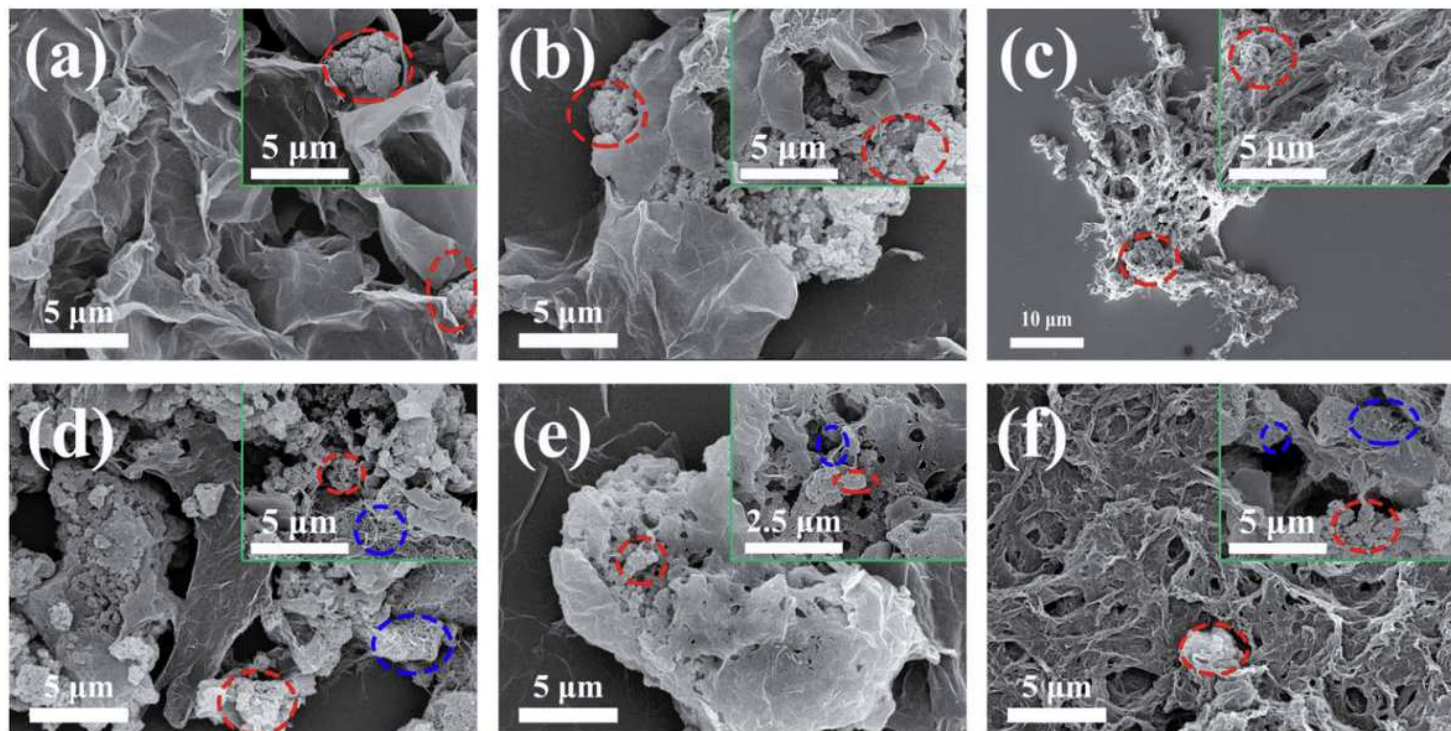


Figure 1

SEM images of PG-*i* (*i* = 2, 4, 5) (a-c) and PCG-*i* (*i* = 2, 4, 5) (d-f).

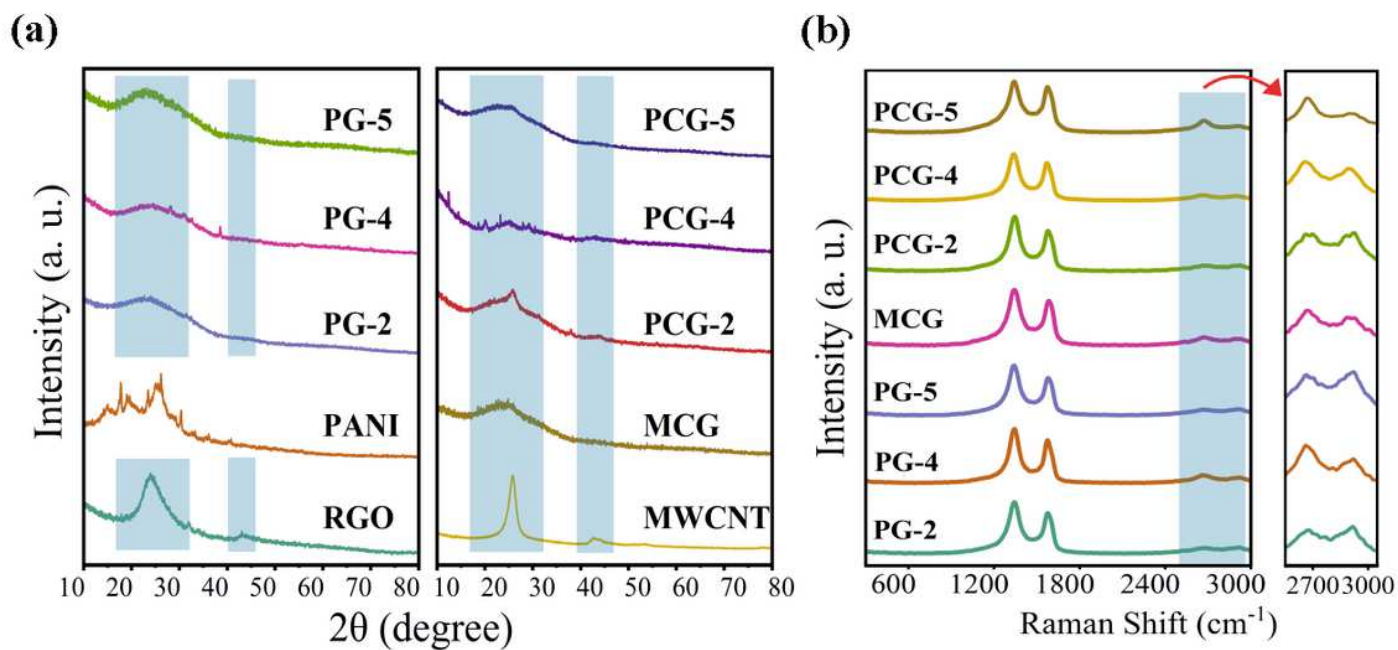
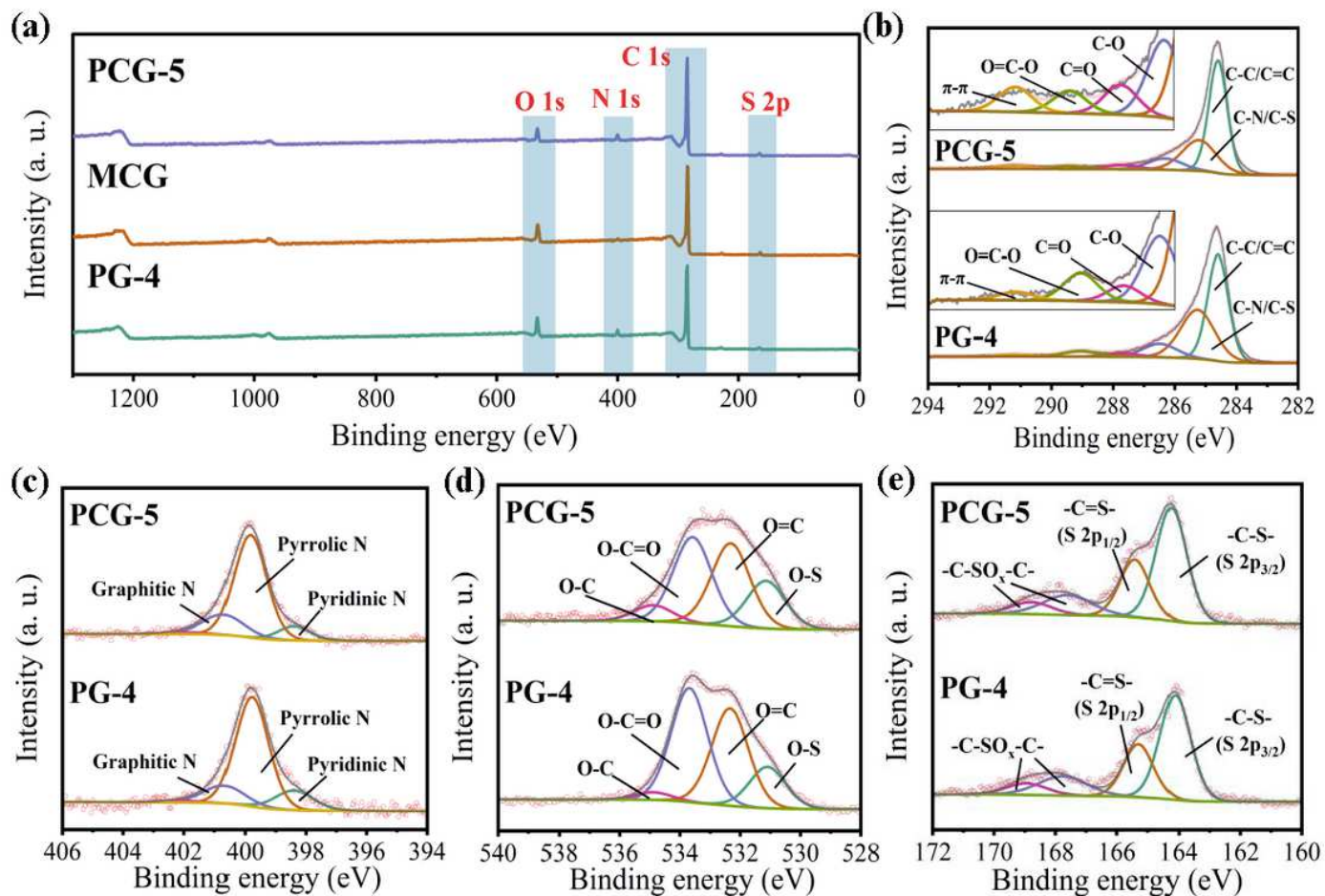


Figure 2

XRD patterns of RGO, PANI, MWCNT, MCG, PG-*i* (*i* = 2, 4, 5) and PCG-*i* (*i* = 2, 4, 5) (a), and Raman spectra of PG-*i* (*i* = 2, 4, 5), MCG and PCG-*i* (*i* = 2, 4, 5) (b).



**Figure 3**

XPS survey spectra of PG-4, MCG and PCG-5 (a), the high-resolution C 1s spectra (b), the high-resolution N 1s spectra (c), the high-resolution O 1s spectra (d), the high-resolution S 2p spectra (e) of PG-4 and PCG-5.

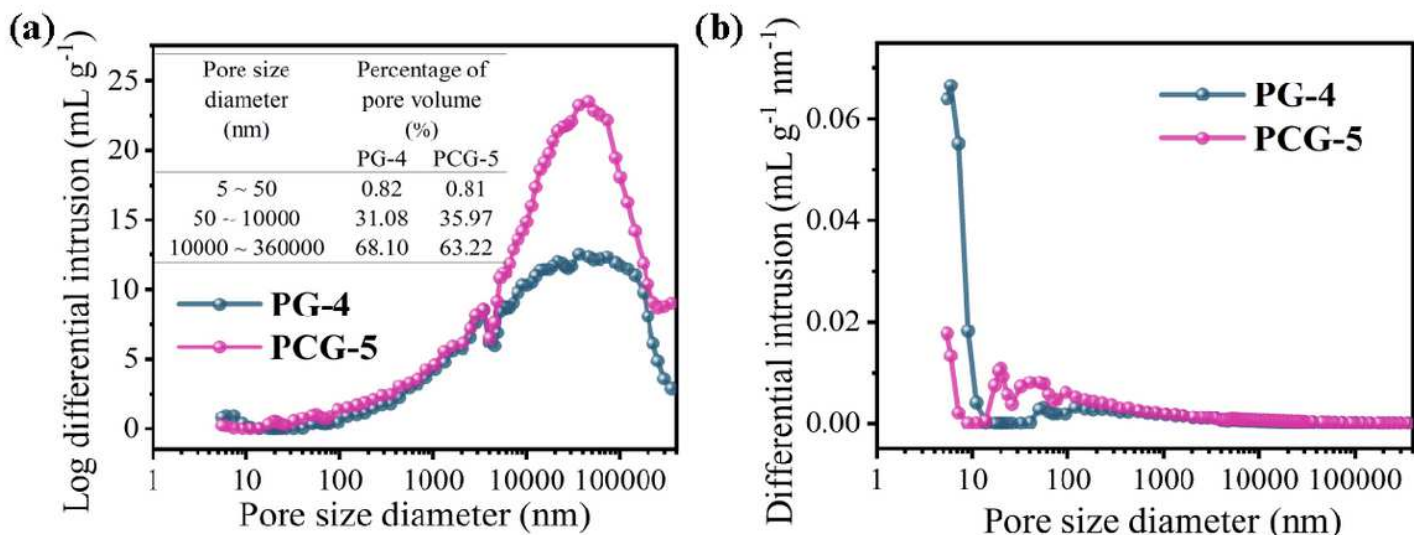


**Figure 4**

Pore-size distribution (a), and pore length distribution (b) of PG-4 and PCG-5.

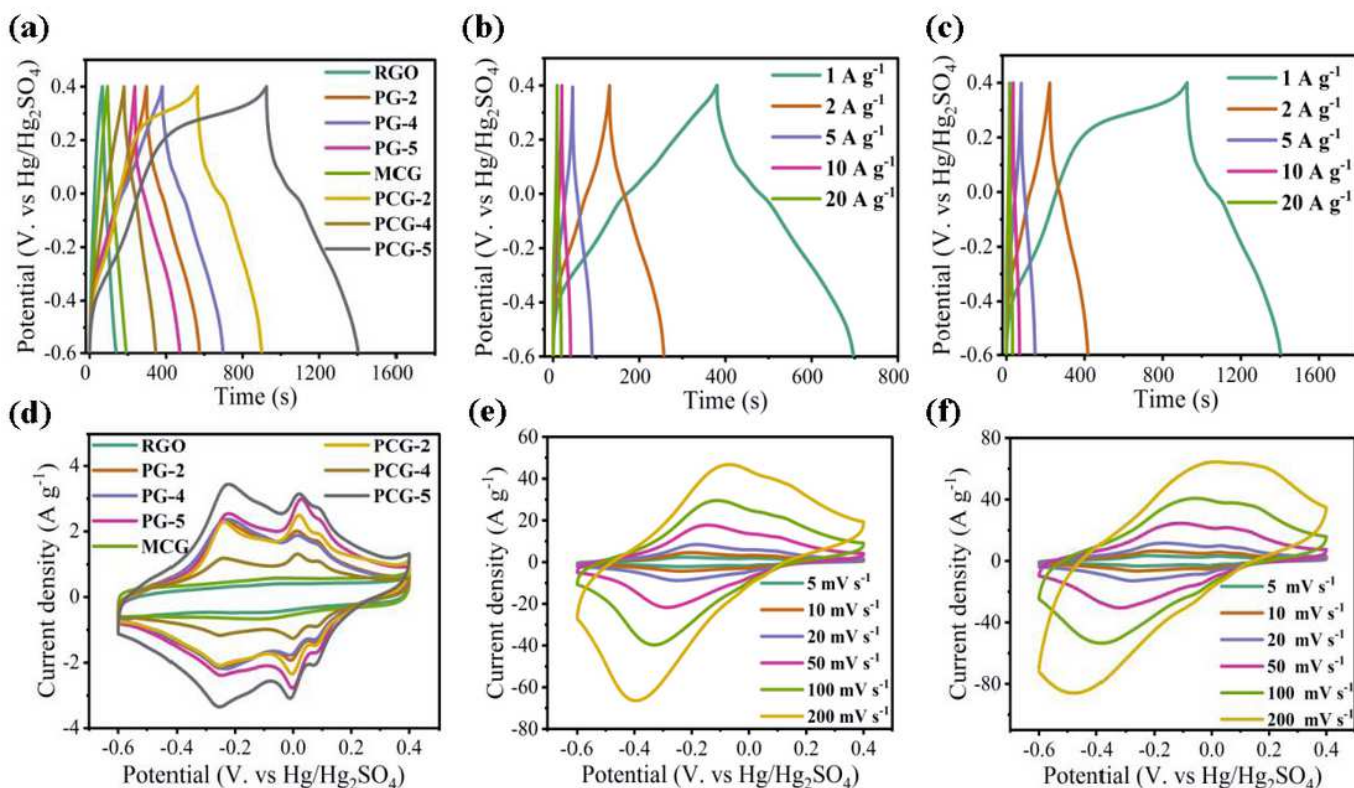


**Figure 5**

GCD curves of RGO, PG-*i* (*i* = 2, 4, 5), MCG and PCG-*i* (*i* = 2, 4, 5) at 1 A g<sup>-1</sup> (a), GCD curves of PG-4 and PCG-5 at different current densities (b~c), CV curves of RGO, PG-*i* (*i* = 2, 4, 5), MCG and PCG-*i* (*i* = 2, 4, 5) at 5 mV s<sup>-1</sup> (d), CV curves of PG-4 and PCG-5 at different scan rates (e~f).

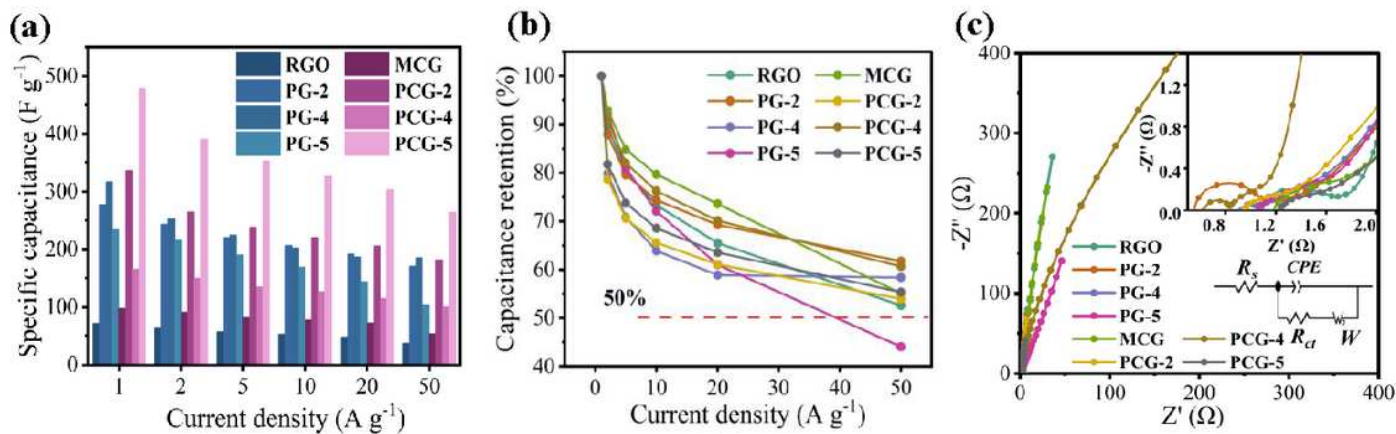


Figure 6

The calculated  $C_m$  at different current densities (a), the capacitance retention (b), and the EIS curves (c) of RGO, MCG, PG- $i$  ( $i = 2, 4, 5$ ) and PCG- $i$  ( $i = 2, 4, 5$ ).

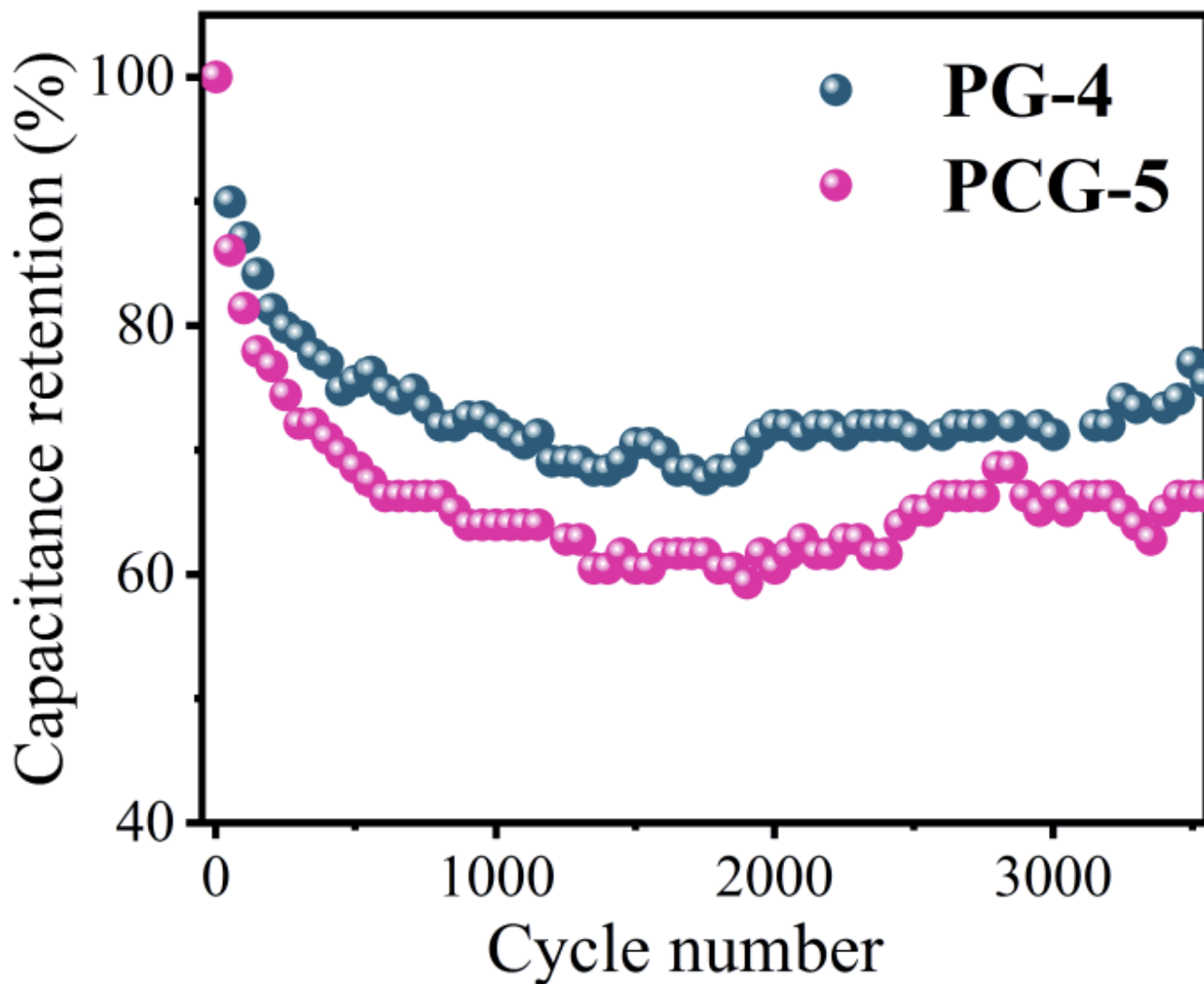


Figure 7

Capacitance retention of PG-4 and PCG-5 after 3500 cycles of continuous charging and discharging at 2 A g<sup>-1</sup>.

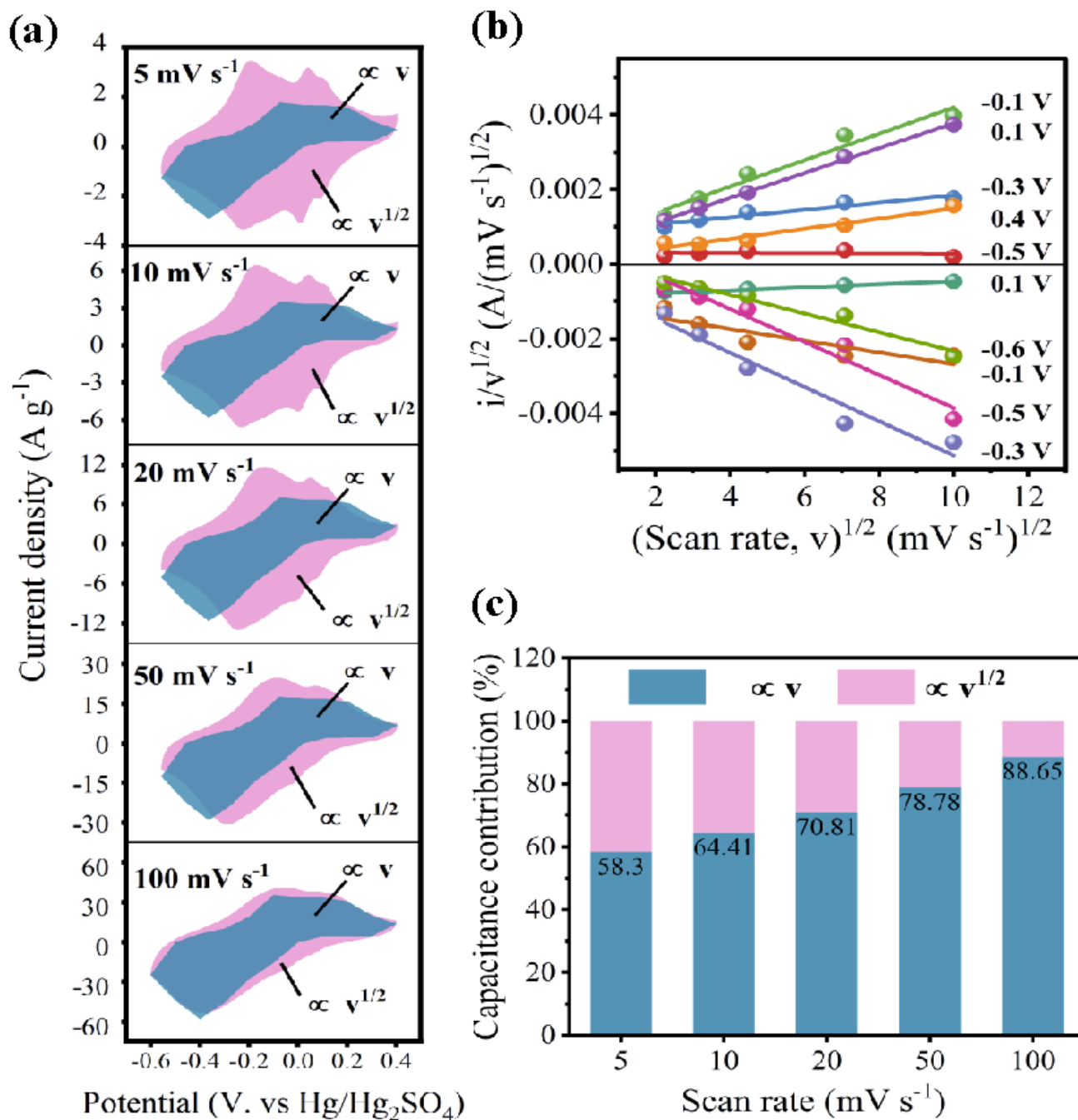


Figure 8

Deconvoluted surface-limiting capacitance ( $\propto v$ , blue region) and diffusion-controlled capacitance ( $\propto v^{1/2}$ , purple region) of PCG-5 at different scan rates (a),  $i/v^{1/2}$  vs  $v^{1/2}$  plots of PCG-5 at different potentials (b), the contribution percentage of the capacitive and diffusion-controlled process at different scan rates of PCG-5 (c).

## Supplementary Files

This is a list of supplementary files associated with this preprint. Click to download.

- [FigS1.png](#)
- [FigS2.png](#)